

Variational Approach to Projected Entangled Pair States at Finite Temperature

Piotr Czarnik¹ and Jacek Dziarmaga¹

¹*Instytut Fizyki Uniwersytetu Jagiellońskiego, ul. Łojasiewicza 11, 30-348 Kraków, Poland*
(Dated: July 8, 2015)

The projected entangled-pair state (PEPS) ansatz can represent a thermal state in a strongly correlated system. We introduce a novel variational algorithm to optimize this tensor network whose essential ingredient is an auxiliary tree tensor network (TTN). Since full tensor environment is taken into account, with increasing bond dimension the PEPS-TTN ansatz provides the exact Gibbs state. Our presentation opens with a 1D version for a matrix product state (MPS-TTN) and then generalizes to PEPS-TTN in 2D. Benchmark results in the quantum Ising model are presented.

PACS numbers: 03.67.-a, 03.65.Ud, 02.70.-c, 05.30.Fk

I. INTRODUCTION

Since their conception as the density matrix renormalization group (DMRG) [1] – an algorithm to optimize the matrix product state (MPS) ansatz in 1D [2] – tensor networks proved to be a competitive tool to study strongly correlated quantum systems. In the last decade, MPS was generalized to a 2D projected entangled pair state (PEPS) [3] and supplemented with an alternative multi-scale entanglement renormalization ansatz (MERA) [4]. These tensor networks avoid the notorious fermionic sign problem [5] and PEPS was applied to the t-J model of high- T_c superconductivity providing the best results on the market [6]. The networks – both MPS [7, 8] and PEPS [9–11] – also made some major breakthroughs in search for topological order.

Unlike the ground state, thermal states were explored mainly with MPS in 1D [12, 13] where they can be prepared by imaginary time evolution. One can follow similar lines in 2D [14, 15] – the PEPS manifold is an efficient representation for Gibbs states [17] – but accurate evolution is more demanding. Alternative direct contractions of the partition function were proposed [16] but – due to local tensor update – they are not warranted to become exact with increasing refinement parameter. In the following we introduce a variational algorithm to optimize PEPS at finite temperature that both employs full tensor update and avoids direct imaginary time evolution.

II. PURIFICATION OF THERMAL STATES

We consider spins on an infinite lattice with a Hamiltonian \mathcal{H} . Every spin has states $s = 0, \dots, S-1$ and is accompanied by an ancilla with states $a = 0, \dots, S-1$. The enlarged “spin+ancilla” space is spanned by states $\prod_m |s_m, a_m\rangle$ where m numbers lattice sites. The Gibbs state of spins at an inverse temperature β is obtained from its purification $|\psi(\beta)\rangle$ in the enlarged space,

$$\rho(\beta) \propto \text{Tr}_{\text{ancillas}} |\psi(\beta)\rangle \langle \psi(\beta)|. \quad (1)$$

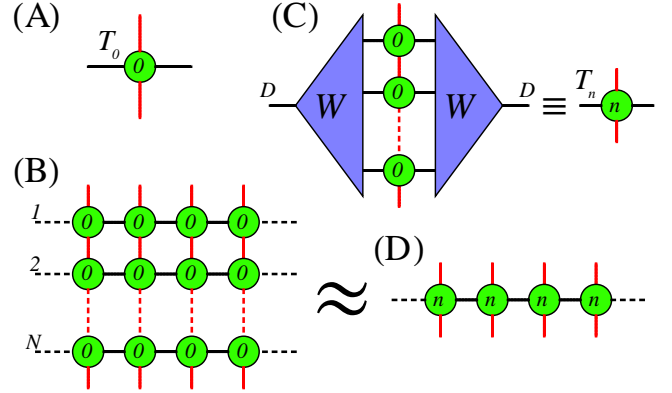


FIG. 1. In A, the Trotter tensor T_0 in 1D. This spin operator with (red) spin indices depends on (black) bond indices connecting it with similar operators at the nearest neighbor sites. In B, evolution operator $U(\beta)$ is a product of N time steps represented by horizontal rows of tensors. Each connecting line is a contracted index. In C, at every site the column of elementary T_0 's is compressed by an isometry W into one tensor T_n with a bond dimension $D < 2^N$. In D, evolution operator $U(\beta)$ is approximated by a matrix product operator of the compressed tensors T_n .

At $\beta = 0$ we choose a product over lattice sites,

$$|\psi(0)\rangle = \prod_m \sum_{s=0}^{S-1} |s_m, s_m\rangle, \quad (2)$$

to initialize the imaginary time evolution,

$$|\psi(\beta)\rangle = e^{-\frac{1}{2}\beta\mathcal{H}} |\psi(0)\rangle \equiv U(\beta) |\psi(0)\rangle. \quad (3)$$

Here the Hermitian $U(\beta) = e^{-\frac{1}{2}\beta\mathcal{H}}$ acts in the Hilbert space of spins. With the initial state (2) the trace in Eq. (1) yields

$$\rho(\beta) \propto U(\beta) U(\beta). \quad (4)$$

In the following the operator $U(\beta)$ will be represented by a projected entangled-pair operator (PEPO). Thanks

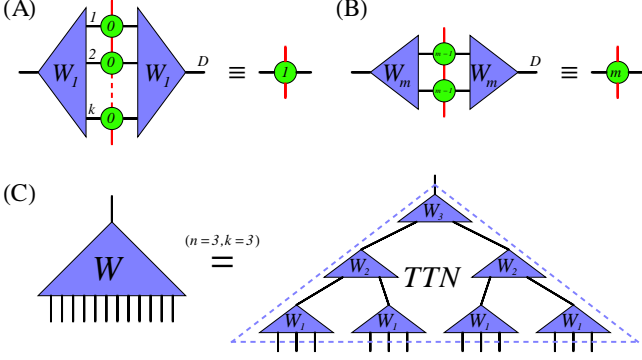


FIG. 2. The huge compression in Fig. 1C is split into n steps. In A, as a first step k elementary Trotter tensors T_0 are compressed by isometry W_1 into tensor T_1 with a bond dimension $D \leq 2^k$. In B, the first step is followed by iterative compressions $T_{m-1} \rightarrow T_m$ preserving the bond dimension D . In C, the final T_n is the same as if the huge isometry W were a tree tensor network (TTN) with n layers of isometries: W_1, \dots, W_n . Here we show an example with $k = 3$ and $n = 3$.

to the simple Eq. (2) equation 3) translates between the PEPO and a PEPS for the purification $|\psi(\beta)\rangle$ in a trivial way: to obtain the PEPO it is enough to rebrand the PEPS's ancilla indices as spin indices.

III. QUANTUM ISING MODEL

We proceed with the quantum Ising model:

$$\mathcal{H} = - \sum_{\langle m, m' \rangle} Z_m Z_{m'} - h \sum_m X_m. \quad (5)$$

Here Z, X are Pauli matrices and h is a transverse field. In 1D, the model has a quantum critical point at $h = 1$ that becomes a crossover at finite temperature. On a 2D square lattice, there is a ferromagnetic phase for small h and large β . At zero temperature the quantum critical point is $h_0 = 3.044$, see Ref. [20], and at $h = 0$ the Onsager's critical point is $\beta_0 = -\ln(\sqrt{2} - 1)/2 = 0.441$. Lattice symmetries are not broken in any phase.

IV. SUZUKI-TROTTER DECOMPOSITION

We define gates

$$U_{ZZ}(\beta) \equiv \prod_{\langle m, m' \rangle} e^{\frac{\beta}{2} Z_m Z_{m'}}, \quad U_X(\beta) \equiv \prod_m e^{\frac{\beta}{2} h X_m}. \quad (6)$$

In the second-order Suzuki-Trotter decomposition a small time step is approximated by their product

$$U(d\beta) \approx U_X(d\beta/2) U_{ZZ}(d\beta) U_X(d\beta/2). \quad (7)$$

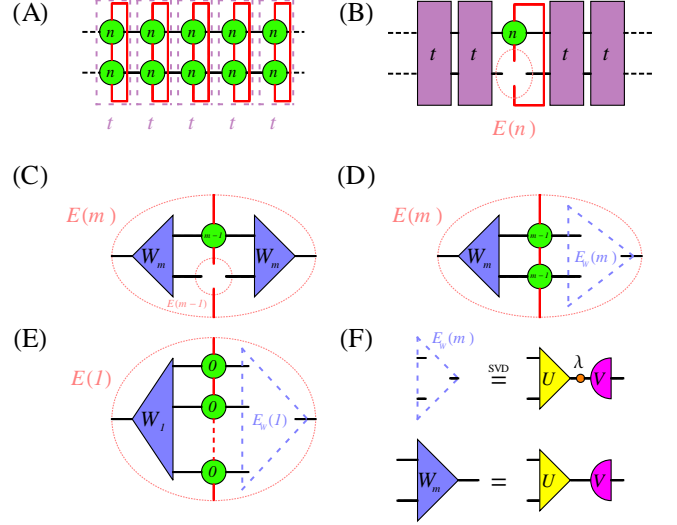


FIG. 3. In A, the partition function $Z = \langle \psi(\beta) | \psi(\beta) \rangle$ is a product of transfer matrices t . In B, the same as in A but with one of the tensors T_n removed. This diagram is the tensor environment $E(n)$ for T_n . In C, a lower-level environment $E(m-1)$ for T_{m-1} is obtained from $E(m)$. In D, environment $E_W(m)$ for isometry W_m is obtained from $E(m)$. In E, environment $E_W(1)$ is obtained from $E(1)$. In F, isometric environment is subject to singular value decomposition, $E_W(m) = U\lambda V^\dagger$, with D non-zero singular values λ , a $D^2 \times D$ isometry U , and a $D \times D$ unitary V . The isometry is updated as $W_m = UV^\dagger$ to maximize the figure of merit $Z = \text{Tr } E_W(m) W_m^\dagger$.

In order to rearrange $U(\beta)$ as a tensor network, at each bond we make a singular value decomposition

$$e^{\frac{d\beta}{2} Z_m Z_{m'}} = \sum_{b=0,1} z_{m,b} z_{m',b}. \quad (8)$$

Here b is a bond index and $z_{m,b} \equiv \sqrt{\Lambda_b} (Z_m)^b$ with the singular values $\Lambda_0 = \cosh \frac{d\beta}{2}$ and $\Lambda_1 = \sinh \frac{d\beta}{2}$. Now we can write

$$U(d\beta) = \sum_{\{b\}} \prod_m \left(e^{\frac{d\beta}{4} h X_m} \prod_{m'} z_{m,b_{\langle m, m' \rangle}} e^{\frac{d\beta}{4} h X_{m'}} \right). \quad (9)$$

Here $\{b\}$ is a set of all bond indices $b_{\langle m, m' \rangle}$. The brackets enclose an elementary Trotter tensor T_0 at site m . It is a spin operator depending on bond indices connecting its site with its nearest neighbors. Its 1D version is shown in Fig. 1A.

The evolution is a product of N small time steps,

$$U(\beta) = [U(d\beta)]^N. \quad (10)$$

For pedagogical reasons, we begin with a 1D version of this product in Fig. 1B, where each row $1 \dots N$ is the elementary time step $U(d\beta)$ and each column is a site in the 1D chain. We need an efficient algorithm to make this huge sum.

V. MPS-TTN ALGORITHM IN 1D

The general idea is to compress first the N elementary tensors T_0 at every site into a single tensor T_n as in Fig. 1C and then to contract the compressed T_n 's horizontally as in Fig. 1D. Here W is an isometry from the auxiliary Hilbert space spanned by 2^N possible values of N bond indices to its D -dimensional subspace. The bond dimension D is a refinement parameter: with increasing D results should become numerically exact.

Furthermore, instead of making the huge compression W all at once – that is all but possible – we split it into n steps as in Figs. 2A, 2B. The final T_n is the same as if W were a tree tensor network (TTN) [18] with n layers of isometries W_1, \dots, W_n , see the example in Fig. 2C. Notice that the number of different isometries is only logarithmic in the number $N = 2^{n-1}k$ of time steps $d\beta$:

$$n = 1 + \log_2 \frac{N}{k} \sim \log N = \log \frac{\beta}{d\beta}. \quad (11)$$

Low temperatures or near-infinitesimal $d\beta$ required in precise applications can be achieved with a marginal logarithmic cost. In the following we describe how this variational TTN ansatz can be optimized in an efficient way.

The optimization aims to maximize the partition function

$$Z[W] = e^{-\beta F} = \text{Tr } e^{-\beta \mathcal{H}} = \text{Tr } U(\beta)U(\beta) \quad (12)$$

with respect to the isometries W_1, \dots, W_n . This figure of merit has to be maximized in order to minimize the Gibbs free energy F . With each $U(\beta)$ in Eq. (4) represented by the diagram in Fig. 1D, Z becomes the tensor network in Fig. 3A.

In order to maximize Z with respect to W_m we need a gradient $\partial Z / \partial W_m$. In principle, the gradient is an infinite sum of derivatives with respect to every W_m in Z but, thanks to the symmetries, all these derivatives are the same and equal to a tensor environment $E_W(m)$ of W_m . The environment is the partition function in Fig. 3A, but with one tensor W_m removed.

The environment can be computed efficiently by an algorithm made of the procedures depicted in Figs. 3B-E. In Fig. 3B we show an environment $E(n)$ for the compressed tensor T_n . This environment is the partition function in Fig. 3A, but with one tensor T_n removed. It can be calculated with the standard transfer-matrix techniques applied to the transfer matrix t . Figure 3C shows how to compute an environment $E(m-1)$ for tensor T_{m-1} from a higher-level environment $E(m)$ for T_m . Repeating this procedure for $m = n, \dots, 2$ we could obtain all Trotter tensors' environments from $E(n-1)$ down to $E(1)$ in one go. However, after each $E(m)$ is obtained we pause to calculate an environment $E_W(m)$ for the isometry W_m by contracting the diagram in Fig. 3D or its variant in Fig. 3E for $m = 1$. This environment is used immediately to optimize W_m by the SVD technique depicted in Fig. 3F. With the updated W_m the algorithm proceeds to calculation of $E(m-1)$ and so forth

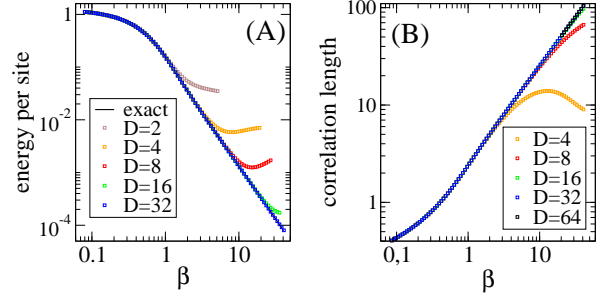


FIG. 4. In A, energy per site of the quantum Ising chain at the critical field $h = 1$ in function of β for different bond dimensions D . For larger D the results remain accurate down to lower temperatures that are closer to the quantum critical point. In B, the correlation length in the tail of the ferromagnetic correlator (13). In both A and B, the number of isometry layers $n = 11$, the bond dimension $D = 2^k = 2, \dots, 64$, and the elementary time step in the Suzuki-Trotter decomposition $d\beta = \beta / (2^{n-1}k)$.

all the way down to $E(1)$ and W_1 when the down optimization sweep is finally completed. The end of the down sweep is the beginning of an up sweep whose first step is calculation of T_1 as in Fig. 2A. With T_1 we calculate $E_W(2)$ contracting the diagram in Figure 3D and then immediately update W_2 before proceeding to calculation of T_2 . This procedure is repeated all the way up to W_n and T_n when the up sweep is completed. Before the next down sweep the environment $E(n)$ in Fig. 3B is updated. The whole optimization procedure is repeated until convergence.

In summary, the variational TTN is optimized by repeated up- and down-sweeps. The up-sweep is a sequence

$$T_0 \rightarrow E_W(1) \rightarrow T_1 \rightarrow \dots \rightarrow E_W(n) \rightarrow T_n \rightarrow E(n)$$

followed by the down sweep

$$E(n) \rightarrow E_W(n) \rightarrow E(n-1) \rightarrow \dots \rightarrow E(1) \rightarrow E_W(1).$$

Each environment $E_W(m)$ is used immediately to update W_m . Progress of the optimization is monitored with a set of figures of merit $Z_m = \text{Tr } E_W(m)W_m^\dagger$. When all Z_m become the same within presumed numerical accuracy, then the isometries are accepted as converged. The numerical cost of the 1D algorithm scales like $(D^2)^3$, where D^2 is the bond dimension of the transfer matrix t .

VI. BENCHMARK RESULTS IN 1D

We applied the algorithm to scan thermal states at the critical field $h = 1$ up to $\beta \approx 40$, see Fig. 4 where we show the energy per site and the correlation length ξ in the ferromagnetic correlator

$$C_R = \langle Z_x Z_{x+R} \rangle - \langle Z_x \rangle \langle Z_{x+R} \rangle \quad (13)$$

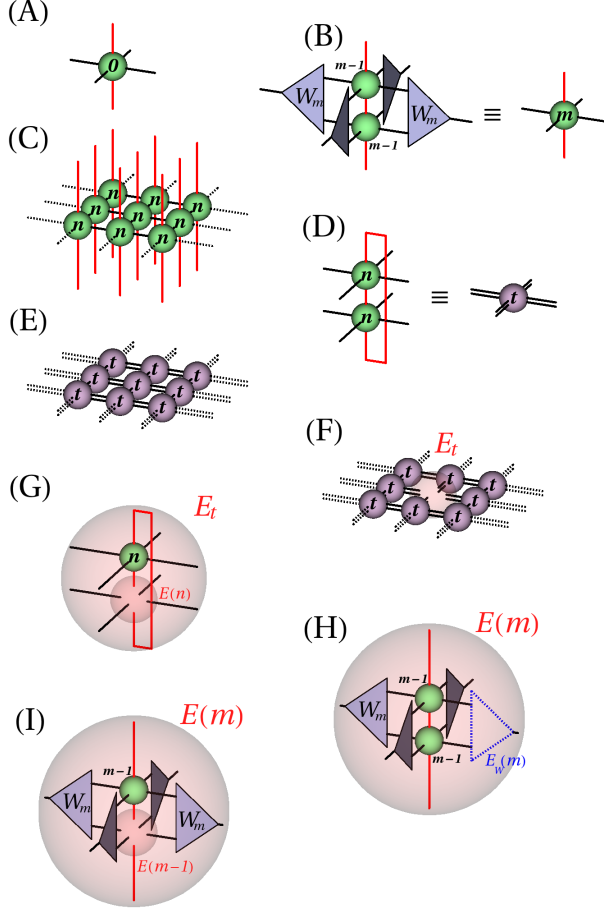


FIG. 5. In A, the elementary Trotter tensor T_0 on a square lattice. In B, compression of two tensors T_{m-1} into one T_m with four isometries W_m . In C, tensors T_n are contracted into a PEPS network for the evolution $U(\beta)$. In D, a contraction of two tensors T_n makes a transfer tensor t . In E, contraction of transfer tensors is the partition function Z . In F, the partition function with one of the transfer tensors removed is a tensor environment E_t for the removed tensor t . We enclose the ends of the free bonds by a transparent reddish sphere. Each free bond has dimension D^2 . In G, when the environment/sphere E_t is filled and contracted with one Trotter tensor T_n we obtain tensor environment $E(n)$ for T_n . This environment is the partition function with one T_n removed. In H, environment $E(m)$ filled and contracted with two T_{m-1} 's and three W_m 's makes environment $E_W(m)$ for isometry W_m . In I, $E(m-1)$ is obtained from $E(m)$.

with an exponential tail $C_R \propto e^{-R/\xi}$ for large R . We find that for increasing bond dimension $D = 2^k$ results remain accurate down to lower temperatures, reaching closer to the quantum critical point.

The number of TTN layers was fixed at $n = 11$ to achieve small enough $d\beta$ for the results to be converged in $d\beta$ all the way down to $\beta \approx 40$. Increasing n up to 20 did not affect stability of the algorithm. The plots in Fig. 4 are scans in increasing β in the sense that isometries

converged for one β were used as the initial isometries for the next $\beta + \delta\beta$. This recycling reduced the number of optimization sweeps necessary for each β to 10...100. This number increased with β as the quantum critical point was approached.

VII. PEPS-TTN ALGORITHM IN 2D

The algorithm can be generalized to a 2D square lattice as summarized in Figure 5. The elementary Trotter tensor T_0 now has four bond indices to be contracted with its four nearest neighbors, see Fig. 5A. Accordingly, each compression of two Trotter tensors T_{m-1} into a higher level tensor T_m is done with four isometries W_m , see Fig. 5B. After all the isometric compressions are completed, the operator $U(\beta)$ can be represented by the PEPO in Fig. 5C with tensors T_n . A contraction of two T_n 's makes a transfer tensor t , see Fig. 5D. The infinite network of transfer tensors in Fig. 5E represents the partition function Z . This 2D network replaces the 1D chain of transfer matrices in Fig. 3A. When one of the transfer tensors in Fig. 5E is removed from the partition function, then we obtain its tensor environment E_t represented by the network in Fig. 5F.

Unlike its analogue in 1D, where the exact transfer-matrix techniques can be used, this environment requires more sophisticated technology. In this paper we use the symmetric version of the corner matrix renormalization (CMR) [19] whose description and discussion is delegated to appendix A. Numerically it is the most expensive part of the algorithm with an additional refinement parameter of its own: the environmental bond dimension M .

Once E_t is converged, we can continue with the main loop of the algorithm. In Fig. 5G E_t is contracted with T_n to yield an environment for T_n that we call briefly $E(n)$. With $E(n)$ the down optimization sweep begins that proceeds as follows. From $E(n)$ we obtain an environment $E_W(n)$ for the isometry W_n as in Fig. 5H. Once calculated, this environment is used immediately to update W_n as in Fig. 3F. With the updated W_n we proceed to calculate the environment $E(n-1)$ for T_{n-1} as in Fig. 5I and then $E_W(n-1)$ to update W_{n-1} . The same procedure repeats all the way down to W_1 .

After all the isometries were optimized down to W_1 , the upwards optimization sweep begins. It has n steps. In the m -th step two tensors T_{m-1} and the environment $E(m)$ – that was calculated before during the down sweep – are contracted to obtain $E_W(m)$, see Fig. 5H. With this environment W_m is updated immediately and then used to compress two T_{m-1} into one T_m as in Fig. 5B. This basic step is repeated all the way up to T_n .

Just as in 1D, the above description can be briefly summarized as follows. The up-sweep is a sequence

$$T_0 \rightarrow E_W(1) \rightarrow T_1 \rightarrow \dots \rightarrow T_{n-1} \rightarrow E_W(n) \rightarrow T_n$$

completed with the CMR procedure

$$T_n \rightarrow E_t \rightarrow E(n).$$

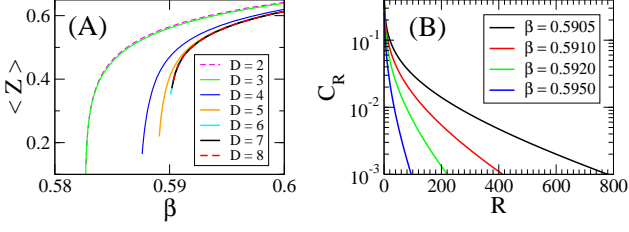


FIG. 6. In A, spontaneous magnetization $\langle Z \rangle$ in the ferromagnetic phase at the transverse field $h = \frac{2}{3}h_0$. Different colors correspond to bond dimensions $D = 2 \dots 8$. Plots for $D = 6, 7, 8$ collapse demonstrating convergence for $D \geq 6$. In B, the ferromagnetic correlator C_R in Eq. (15) for $D = 6$ at $h = \frac{2}{3}h_0$ and different β in the ferromagnetic phase. Its correlation length diverges closer to criticality requiring a diverging M . For $M = 68$ the longest length achieved is $\xi = 290$ lattice sites.

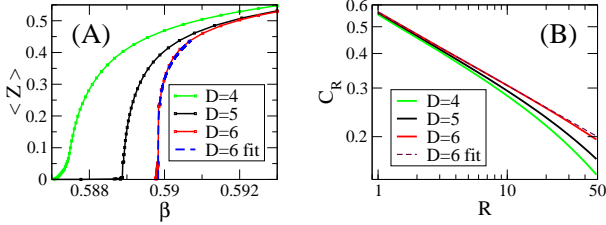


FIG. 7. In A, spontaneous magnetization $\langle Z \rangle$ near the critical point. With increasing bond dimension D the plots become “critical” enough to make a fit $\langle Z \rangle \propto (\beta - \beta_c)^{\beta'}$ with a critical-point $\beta_c = 0.5898$ and a critical exponent $\beta' = 0.198$. In B, the ferromagnetic correlation function (15) for $D = 6$ at β_c . In the intermediate range $1 < R < 30$ the correlator is fitted well by the power law $C_R \propto R^{-\eta}$ with the critical exponent $\eta = 0.265$.

that is also the starting point for the down-sweep,

$$E(n) \rightarrow E_W(n) \rightarrow E(n-1) \rightarrow \dots \rightarrow E(1) \rightarrow E_W(1).$$

Here, both in the up- and down-sweeps, each $E_W(m)$ is used immediately to update W_m . The whole up-down cycle is repeated until convergence.

The numerical cost of the procedures in panels B,D,G,H,I of Fig. 5 scales formally like $(D^2)^4$, where D^2 is the bond dimension of the transfer tensor. The exponent is steeper than in 1D, but a much smaller D is typically needed in 2D. For instance, unlike in 1D, D can be finite at a critical point. However, the actual bottleneck is the CMR in appendix A, whose cost scales like $(D^2)^3 M^3$. In non-symmetric versions of CMR [19] this formal cost can be cut down to $(D^2)^2 M^3$. The parameter M is expected to diverge at a critical point together with a diverging correlation length but, even at criticality, local observables and correlations at increasingly long distance can be converged with increasing M .

VIII. BENCHMARK RESULTS IN 2D

We applied the PEPS-TTN algorithm to scan the ferromagnetic phase at the transverse field

$$h = \frac{2}{3}h_0. \quad (14)$$

Results in Fig. 6 show convergence in the bond dimension (for $D \geq 6$). For each D they are converged in the environmental bond dimension M . The plots do not extend all the way down to the critical point, because the diverging correlation length would require a diverging environmental bond dimension M to obtain a Gibbs state fully converged in M . Nevertheless, even with a limited $M \leq 68$ we could get close enough to the critical point to obtain a converged ferromagnetic correlation function

$$C_R = \langle Z_{x,y} Z_{x+R,y} \rangle - \langle Z_{x,y} \rangle \langle Z_{x+R,y} \rangle \quad (15)$$

with a long correlation length up to $\xi = 290$ in its exponential tail $C_R \propto e^{-R/\xi}$ for large R .

The plots in Fig. 6 are fully converged in M , but they terminate before the critical point provoking a natural question what, if anything, can be achieved closer to criticality. Hence we pushed our computations closer, accepting the fact that the ansatz cannot be fully converged there. Results are shown in Fig. 7. The spontaneous magnetization for $D = 6$ and $M = 35$ allows a power law fit that gives the order parameter exponent $\beta' = 0.198$ (the textbook exponent β distinguished here by a prime from the inverse temperature) and the critical point $\beta_c = 0.5898$. The correlation function at β_c has an exponential tail that is not converged in M – its range increases with M – but at an intermediate range $1 < R < 30$ the correlator has the correct form $C_R \propto R^{-\eta}$ with the critical exponent $\eta = 0.265$.

To give an idea about practical effectiveness of the algorithm, it would take 1 day on a 4-core laptop computer to reproduce Fig. 6 and, since the convergence is slower near criticality, 2-3 more days for Fig. 7. Our TTN had $n = 6$ layers of isometries with $k = 5$ in the bottom layer. The computation time was checked to be practically independent of n , as it is CMR that is the actual bottle-neck and not the isometry optimizations. For random initial conditions, the number of up- and down- optimization sweeps necessary to reach convergence was $\simeq 100$. For a scan in β – when tensors converged for one β were recycled as initial tensors at a near $\beta - \delta\beta$ – the number of sweeps was typically $\simeq 10$. Both numbers increased towards the critical point.

IX. COMPARISON WITH DIRECT IMAGINARY TIME EVOLUTION

In our previous work [14, 15], we made efforts to obtain thermal states by direct imaginary time evolution from $\beta = 0$ to a finite one. In Fig. 8 we compare our

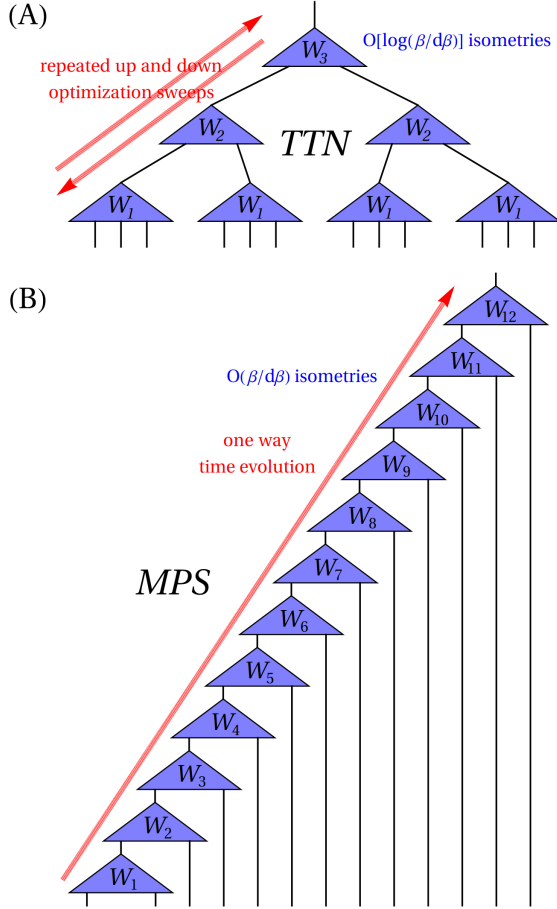


FIG. 8. Comparison between the present variational method in A and the direct imaginary time evolution in B. The TTN ansatz is exponentially more compact than MPS since the number of different isometries is only logarithmic in the number of time steps. On top of this, in the present variational method the isometries in TTN are optimized by repeated up- and down-sweeps to provide only the most accurate state at the final β , while in the time evolution all intermediate states between 0 and the final β need to be accurate compromising the accuracy of the final one.

present method with the time evolution. The most striking difference is the ansatz for the huge isometry W . In the time evolution we apply one elementary Trotter tensor T_0 at every time step. Every application is followed by a renormalization of the PEPS tensor with a new isometry W_m . This procedure implicitly assumes the (left-canonical) matrix product state (MPS) ansatz in Fig. 8B. It has $\mathcal{O}(\beta/d\beta)$ different isometries, while in the corresponding TTN in Fig. 8A the same number is only $\mathcal{O}[\log(\beta/d\beta)]$. This is a dramatic difference for large β or precise applications that require infinitesimal $d\beta$.

Another, possibly less apparent, difference is the optimization procedure. In the time evolution it is a one way process. After the m -th time step we choose the optimal isometry W_m to renormalize the bond indices of

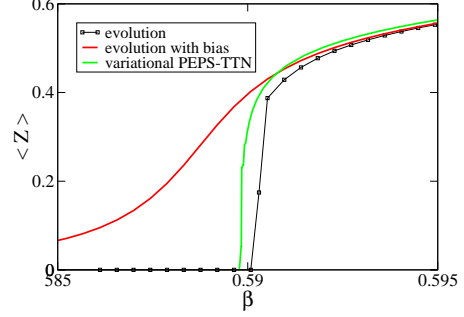


FIG. 9. Spontaneous magnetization $\langle Z \rangle$ in function of β obtained with different algorithms. The direct imaginary time evolution produces a plot with a discontinuity near the second order transition due to insufficient M . Adding a tiny symmetry breaking bias $\delta = 10^{-6}$ smooths the transition making the necessary M finite. Both evolution curves come from Ref. [15]. They are compared with the PEPS-TTN curve from Fig. 7A. Here all the results for $D = 6$.

the new PEPS tensor after this step. Once chosen, W_m remains fixed and an error incurred with W_m affects the whole following evolution. The errors accumulate with time. In the present variational approach we assume an entirely different strategy. Instead of scanning the whole range from 0 to β we target only the final β . The isometries are optimized by repeated up- and down-sweeps to provide the best final state. Each isometry alone and the whole set of isometries in tune are serving the single goal to make the targeted state as accurate as possible. Unlike in the time evolution, they are not compromised to provide accurate thermal states at intermediate imaginary times. Even if T_n is the best PEPS tensor at the final β , T_{n-s} does not need to be the best one at β/s .

The last property contributes to the main advantage of the variational PEPS-TTN over time evolution. The variational algorithm can probe a low temperature phase without any need to evolve from infinite temperature across a critical point. Not only there is no direct evolution through intermediate temperatures, but also the intermediate tensors T_{n-s} do not need to be thermal states at all. The problems with evolution across the critical point are illustrated in Figure 9, where we compare three ferromagnetic magnetization curves obtained with three different algorithms. The direct evolution runs into trouble at the critical point, where exact evolution would require a divergent M , and the magnetization makes a discontinuous jump. This problem can be partly circumvented by adding a tiny symmetry breaking bias to the Hamiltonian,

$$\Delta H = -\delta \sum_m Z_m, \quad (16)$$

that smooths the transition making the necessary M finite, but significantly alters the physics at the critical point. Nevertheless, the bias allows smooth evolution

from infinite temperature deep into the low temperature phase, where the effect of the tiny bias becomes negligible. However, even the bias cannot prevent the evolution from accumulating errors with time.

In retrospect, it may be tempting to combine the new variational strategy with the MPS ansatz instead of TTN. After all, the powerful methods developed for MPS [2] may be efficient enough to optimize even the huge number $\mathcal{O}(\beta/d\beta)$ of isometries. Unfortunately, these methods cannot be applied in 2D. Instead, the isometries in MPS have to be optimized by the procedures in Fig. 5 combined with CMR. Since an isometry in MPS maps from $2D$ to D dimensions, rather than from D^2 to D in TTN, the procedures are more efficient for MPS than for TTN. However, the actual bottleneck that limits D on an infinite lattice is the CMR whose cost depends only on the net D and not on the underlying ansatz. Thus with MPS one can achieve the same D as with TTN, but at the expense of an algorithm that is linear instead of logarithmic in $\beta/d\beta$. Apart from this, the linear algorithm has a lot more variational parameters, hence in principle it may be more liable to getting trapped in local maxima of the figure of merit. However, this discussion does not quite exclude MPS in some applications like, e.g., a finite

lattice.

X. CONCLUSION

The proposed PEPS-TTN method is the first 2D finite-temperature tensor-network algorithm that is both variational and becomes numerically exact with increasing bond dimension. It avoids the demanding direct imaginary time evolution and employs full tensor environment in variational optimization. There is still a lot of room for improvement and development. For instance, the simple TTN could be made more powerful with some unitary disentanglers [4]. Internal symmetries, like Z_2 or $U(1)$, could help to use the bond dimension more efficiently. Finally, CMR may be upgraded to an algorithm making more efficient use of the environmental bond dimension.

ACKNOWLEDGMENTS

This work was supported by the Polish National Science Center (NCN) under project DEC-2013/09/B/ST3/01603.

-
- [1] S. R. White, Phys. Rev. Lett. **69**, 2863 (1992).
 - [2] U. Schollwöck, Annals of Physics **326**, 96 (2011).
 - [3] F. Verstraete and J. I. Cirac, cond-mat/0407066; V. Murg, F. Verstraete, and J. I. Cirac, Phys. Rev. A **75**, 033605 (2007); G. Sierra and M. A. Martin-Delgado, arXiv:cond-mat/9811170; T. Nishino and K. Okunishi, J. Phys. Soc. Jpn. **67**, 3066 (1998); Y. Nishio, N. Maeshima, A. Gendiar, and T. Nishino, cond-mat/0401115; J. Jordan, R. Orús, G. Vidal, F. Verstraete, and J. I. Cirac, Phys. Rev. Lett. **101**, 250602 (2008); Z.-C. Gu, M. Levin, and X.-G. Wen, Phys. Rev. B **78**, 205116 (2008); H. C. Jiang, Z. Y. Weng, and T. Xiang, Phys. Rev. Lett. **101**, 090603 (2008); Z. Y. Xie, H. C. Jiang, Q. N. Chen, Z. Y. Weng, and T. Xiang, Phys. Rev. Lett. **103**, 160601 (2009); P.-C. Chen, C.-Y. Lai, and M.-F. Yang, J. Stat. Mech.: Theory Exp. (2009) P10001; R. Orús and G. Vidal, Phys. Rev. B **80**, 094403 (2009).
 - [4] G. Vidal, Phys. Rev. Lett. **99**, 220405 (2007); G. Vidal, Phys. Rev. Lett. **101**, 110501 (2008); L. Cincio, J. Dziarmaga, and M. M. Rams, Phys. Rev. Lett. **100**, 240603 (2008); G. Evenbly and G. Vidal, Phys. Rev. Lett. **102**, 180406 (2009); G. Evenbly and G. Vidal, Phys. Rev. B **79**, 144108 (2009); G. Evenbly and G. Vidal, Phys. Rev. Lett. **112**, 240502 (2014); Phys. Rev. B **89**, 235113 (2014).
 - [5] T. Barthel, C. Pineda, and J. Eisert Phys. Rev. A **80**, 042333 (2009); P. Corboz and G. Vidal, Phys. Rev. B **80**, 165129 (2009); P. Corboz, G. Evenbly, F. Verstraete, and G. Vidal, Phys. Rev. A **81**, 010303(R) (2010); C. V. Kraus, N. Schuch, F. Verstraete, and J. I. Cirac, Phys. Rev. A **81**, 052338 (2010); C. Pineda, T. Barthel, and J. Eisert, Phys. Rev. A **81**, 050303(R) (2010). Z.-C. Gu, F. Verstraete, and X.-G. Wen, arXiv:1004.2563 (2010).
 - [6] P. Corboz, R. Orús, B. Bauer, and G. Vidal, Phys. Rev. B **81**, 165104 (2010); P. Corboz, S. R. White, G. Vidal, and M. Troyer, Phys. Rev. B **84**, 041108 (2011); P. Corboz, T. M. Rice, M. Troyer, Phys. Rev. Lett. **113**, 046402 (2014).
 - [7] S. Yan, D. A. Huse, and S. R. White, Science **332**, 1173 (2011).
 - [8] L. Cincio and G. Vidal, Phys. Rev. Lett. **110**, 067208 (2013).
 - [9] D. Poilblanc, N. Schuch, D. Pérez-García, and J. I. Cirac, Phys. Rev. B **86**, 014404 (2012).
 - [10] D. Poilblanc, N. Schuch, Phys. Rev. B **87**, 140407(R) (2013).
 - [11] L. Wang, D. Poilblanc, Z.-C. Gu, X.-G. Wen, and F. Verstraete, Phys. Rev. Lett. **111**, 037202 (2013).
 - [12] F. Verstraete, J. J. Garcia-Ripoll, and J. I. Cirac, Phys. Rev. Lett. **93**, 207204 (2004); M. Zwolak and G. Vidal, Phys. Rev. Lett. **93**, 207205 (2004); A.E. Feiguin and S.R. White, Phys. Rev. B **72**, 220401 (2005).
 - [13] S. R. White, arXiv:0902.4475; E.M. Stoudenmire and Steven R. White, New J. Phys. **12**, 055026 (2010); I. Pizorn, V. Eisler, S. Andergassen, and M. Troyer, New J. Phys. **16**, 073007 (2014).
 - [14] P. Czarnik, L. Cincio, and J. Dziarmaga, Phys. Rev. B **86**, 245101 (2012); P. Czarnik and J. Dziarmaga, Phys. Rev. B **90**, 035144 (2014).
 - [15] P. Czarnik and J. Dziarmaga, arXiv:1411.6778.
 - [16] Z. Y. Xie, H. C. Jiang, Q. N. Chen, Z. Y. Weng, T. Xiang, Phys. Rev. Lett. **103**, 160601 (2009); H.H. Zhao, Z.Y. Xie, Q.N. Chen, Z.C. Wei, J.W. Cai, T. Xiang, Phys. Rev. B **81**, 174411 (2010); W. Li, S.-J. Ran, S.-S. Gong, Y. Zhao, B. Xi, F. Ye, and G. Su, Phys. Rev. Lett. **106**, 127202 (2011); Z. Y. Xie, J. Chen, M. P. Qin, J. W. Zhu, L. P.

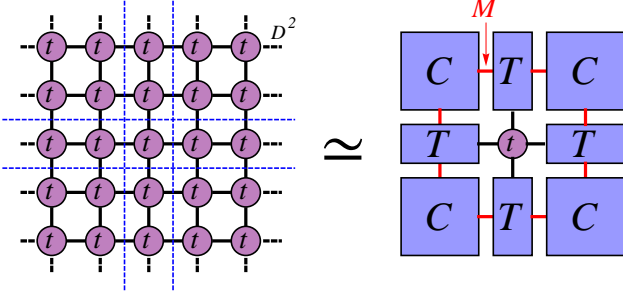


FIG. 10. On the left, a planar version of the network in Fig. 5E representing the partition function. Here each (black) bond represents two bond indices in Fig. 5E. Its dimension is D^2 . This infinite contraction cannot be done exactly, hence it is approximated by the finite network on the right. The finite corner matrices C and top tensors T effectively represent corresponding infinite sectors of the network on the left separated by the dashed blue lines. Their (red) environmental bonds have dimension M . The environmental tensors C and T should be such that to the transfer tensor t in the center its effective environment on the right appears the same as its exact environment on the left as much as possible. They are obtained by iterating until convergence the corner matrix renormalization in Fig. 11.

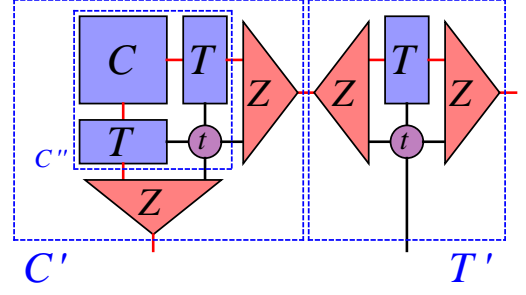


FIG. 11. The corner C and top T are obtained by repeating until convergence a renormalization procedure. The procedure has four steps. In the first step, the tensors C, T, t are contracted to an enlarged corner C'' . In the second step, the symmetric $MD^2 \times MD^2$ matrix C'' is diagonalized and its M eigenvectors with the largest eigenvalues define an isometry Z . The diagonalization that scales like $M^3 D^6$ is the leading cost of this variant of corner matrix renormalization. In the third step, Z is used to renormalize/truncate the indices of C'' back to the original dimension M giving a new (diagonal) corner C' . In the fourth step, the same Z renormalizes the contraction of T with t to a new T' . The four-step procedure is repeated until convergence of the M leading eigenvalues of C'' .

- Yang, and T. Xiang, Phys. Rev. B **86**, 045139 (2012); Shi-Ju Ran, Wei Li, Bin Xi, Zhe Zhang and Gang Su, Phys. Rev. B **86**, 134429 (2012); S.-J. Ran, B. Xi, T. Liu, and G. Su, Phys. Rev. B **88**, 064407 (2013); A. Denbleyker, Y. Liu, Y. Meurice, M. P. Qin, T. Xiang, Z. Y. Xie, J. F. Yu, H. Zou, Phys. Rev. D **89**, 016008 (2014).
- [17] A. Molnár, N. Schuch, F. Verstraete, and J. I. Cirac, arXiv:1406.2973.
- [18] L. Tagliacozzo, G. Evenbly, and G. Vidal, Phys. Rev. B **80**, 235127 (2009).
- [19] R. J. Baxter, J. Math. Phys. **9**, 650 (1968); J. Stat. Phys. **19**, 461 (1978); T. Nishino and K. Okunishi, J. Phys. Soc. Jpn. **65**, 891 (1996); R. Orús and G. Vidal, Phys. Rev. B **80**, 094403 (2009); R. Orús, Phys. Rev. B **85**, 205117 (2012); R. Orús, Ann. of Phys. **349**, 117 (2014); Ho N. Phien, I. P. McCulloch, G. Vidal, arXiv:1411.0391.
- [20] H. Rieger, N. Kawashima, Europ. Phys. J. B **9**, 233 (1999); H.W.J. Blote and Y. Deng, Phys. Rev. E **66**, 066110 (2002).

Appendix A: Corner matrix renormalization (CMR)

An infinite tensor network, like the one in Fig. 5E, cannot be contracted exactly. Fortunately, what we need in general is not this number, but an environment for a few tensors of interest. For instance, in Fig. 5F we want an environment E_t for the transfer tensor t in the center. The environment is a tensor that remains after removing the central tensor t from the infinite network. From the point of view of the central tensor, its infinite environment can be substituted with a finite effective en-

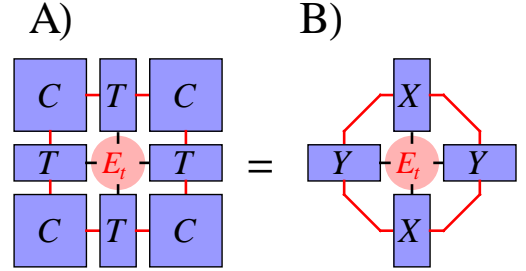


FIG. 12. In A, a finite tensor network approximating the infinite environment E_t in Fig. 5F. Notice that the corner matrix C can be singular-value-decomposed, $C = U\lambda V^\dagger$, and then absorbed into the neighboring top tensors T . With $X = \sqrt{\lambda}U^\dagger T U \sqrt{\lambda}$ and $Y = \sqrt{\lambda}V^\dagger T V \sqrt{\lambda}$ (here the matrix products are understood in the environmental bond indices) we obtain an equivalent network in panel B. This network is a matrix product state (MPS) of four tensors X, Y, X, Y with a bond dimension M , hence in principle a finite M could suffice to represent the exact E_t even at the critical point.

vironment, made of finite corner matrices C and top tensors T , that appears to the central tensor the same as the exact environment as much as possible. The environmental tensors are contracted with each other by indices of dimension M . Increasing M makes the effective environment more accurate and, for a finite correlation length, the effective environment is expected to converge to the exact one at a finite M . In the Ising model, tensor t is symmetric under permutation of its indices and, consequently, C is a symmetric matrix and T is symmetric in its environmental indices.

Finite tensors C and T represent infinite sectors of the network on the left of Fig. 10. The tensors are con-

verged by iterating the corner matrix renormalization in Fig. 11. In every renormalization step, the corner matrix is enlarged with one t and two T 's. This operation represents the top-left corner sector in Fig. 10 absorbing one more layer of tensors t . Once the environment is converged, it can be used to calculate either an observable or the environment E_t , see Fig. 12.

The above CMR procedure requires M that diverges at a critical point. This is clearly demonstrated in the appendix of Ref. [15] at the Onsager transition in the 2D classical Ising model, where a finite M results in a finite correlation length $\propto M^{1.93}$. The tail of the correlation function cannot become strictly algebraic for any finite M but, as illustrated in section VII and Ref. [15], with increasing M not only local observables but also correlations at increasingly long distance become converged in M . At a critical point the effective environment is not exact, but provides an approximation whose quality improves with M in a systematic way.

In an attempt to go beyond this bottom line, one could

argue that the divergent M required at criticality is not an inherent property of the finite effective environment, but an artifact of the specific CMR method used to obtain this environment. Indeed, the exact tensor E_t in Fig. 5F can be interpreted as a quantum state on the four free bonds, each free bond with D^2 auxiliary states. Such a finite state can be represented by a four-site MPS with a finite bond dimension M . In Fig. 12B we show that this MPS is equivalent to a finite effective environment with the same M . This completes the argument that for a finite D the exact E_t can be represented with a finite M .

An exact local E_t is all we need to optimize the isometries W_m of the thermal PEPS, even though the finite M of its exact environmental tensors may prohibit accurate calculation of the power-law tails of critical correlations. The present CMR method attempts to be universal – accurate for both local and non-local observables – while in order to optimize the PEPS tensor all we need is a method targeting the local E_t only.